

blue and black curves, respectively. Here, we performed the computation 100 times; the curves indicating the shortest times needed to reach the target energy are shown for both the CIM and SA. The times needed to reach the target Ising energy were about 70  $\mu\text{s}$  for the CIM and 3.2 ms for SA, implying that the CIM could obtain the benchmark Ising energy more quickly than with SA by a factor of nearly 50. This result suggests that a CIM can outperform SA on a CPU when solving dense graph problems.

According to the numerical study of Maruo *et al.* (14), the formation of a superposed state is observed when an optically coupled CIM is operated in the shot noise–limited regime. This suggests that the CIM may exhibit quantum behavior, although experimental confirmation is yet to be achieved. A more detailed discussion on the quantumness of the CIM is provided in (24).

#### REFERENCES AND NOTES

- R. M. Karp, *Complexity of Computer Computations* (Plenum, 1972), pp. 85–103.
- S. Kirkpatrick, C. D. Gelatt Jr., M. P. Vecchi, *Science* **220**, 671–680 (1983).
- F. Barahona, *J. Phys. A* **15**, 3241–3253 (1982).
- M. W. Johnson *et al.*, *Nature* **473**, 194–198 (2011).
- K. Kim *et al.*, *Nature* **465**, 590–593 (2010).
- I. Mahboob, H. Okamoto, H. Yamaguchi, *Sci. Advances* **2**, e1600236 (2016).
- M. Yamaoka *et al.*, *IEEE J. Solid-State Circuits* **51**, 303–309 (2015).
- S. Utsunomiya, K. Takata, Y. Yamamoto, *Opt. Express* **19**, 18091–18108 (2011).
- Z. Wang, A. Marandi, K. Wen, R. L. Byer, Y. Yamamoto, *Phys. Rev. A* **88**, 063853 (2013).
- M. Wolinsky, H. J. Carmichael, *Phys. Rev. Lett.* **60**, 1836–1839 (1988).
- L. Krippner, W. J. Munro, M. D. Reid, *Phys. Rev. A* **50**, 4330–4338 (1994).
- P. D. Drummond, K. Dechoum, S. Chaturvedi, *Phys. Rev. A* **65**, 033806 (2002).
- K. Takata, A. Marandi, Y. Yamamoto, *Phys. Rev. A* **92**, 043821 (2015).
- D. Maruo, S. Utsunomiya, Y. Yamamoto, *Phys. Scr.* **91**, 083010 (2016).
- A. Marandi, Z. Wang, K. Takata, R. L. Byer, Y. Yamamoto, *Nat. Photonics* **8**, 937–942 (2014).
- T. Inagaki *et al.*, *Nat. Photonics* **10**, 415–419 (2016).
- J. King, S. Yarkoni, M. M. Nevisi, J. P. Hilton, C. C. McGeoch, <http://arxiv.org/abs/1508.05087> (2015).
- E. Ising, *Z. Phys. A* **31**, 253–258 (1925).
- C. D. Nabors, S. T. Yang, T. Day, R. L. Byer, *J. Opt. Soc. Am. B* **7**, 815–820 (1990).
- A. Marandi, N. C. Leindecker, V. Pervak, R. L. Byer, K. L. Vodopyanov, *Opt. Express* **20**, 7255–7262 (2012).
- D. K. Serkland, G. D. Bartolini, A. Agarwal, P. Kumar, W. L. Kath, *Opt. Lett.* **23**, 795–797 (1998).
- Y. Okawachi *et al.*, *Opt. Lett.* **40**, 5267–5270 (2015).
- Y. Haribara, S. Utsunomiya, K. Kawarabayashi, Y. Yamamoto, <https://arxiv.org/abs/1501.07030> (2015).
- See supplementary materials on Science Online.
- M. E. Marhic, C. H. Hsia, J. M. Jeong, *Electron. Lett.* **27**, 210–211 (1991).
- R.-D. Li, P. Kumar, W. L. Kath, *J. Lightwave Technol.* **12**, 541–549 (1994).
- C. Helmberg, F. Rendl, *SIAM J. Optim.* **10**, 673–696 (2000).
- G. Rinaldy, rudy graph generator, [www-user.tu-chemnitz.de/~helmberg/rudy.tar.gz](http://www-user.tu-chemnitz.de/~helmberg/rudy.tar.gz) (1996).
- M. X. Goemans, D. P. Williamson, *J. ACM* **42**, 1115–1145 (1995).

#### ACKNOWLEDGMENTS

Supported by the Impulsing Paradigm Change Through Disruptive Technologies (ImPACT) Program of the Council of Science, Technology and Innovation (Cabinet Office, Government of Japan). We thank H. Nishimori for fruitful discussions, K. Inaba for fruitful discussions, and H. Tamura for various types of support during this research. S.U. and H. Takesue are inventors on patent application PCT/JP2015/059057 submitted by the National

Institute of Informatics (NII) and Nippon Telegraph and Telephone (NTT) Corporation that covers the coherent Ising machine based on the measurement and feedback scheme. A.M. and S.U. are inventors on patent application PCT/US2014/046025 submitted by Stanford University and NII that covers the implementation of a coherent Ising machine using degenerate optical parametric oscillators. T.U., K.E., and H. Takenouchi are inventors on patent application PCT/JP1012/000360 submitted by NTT that covers the configurations of phase-sensitive amplifiers based on periodically poled lithium niobate waveguides.

#### SUPPLEMENTARY MATERIALS

[www.sciencemag.org/content/354/6312/603/suppl/DC1](http://www.sciencemag.org/content/354/6312/603/suppl/DC1)  
Materials and Methods  
Supplementary Text  
Figs. S1 to S5  
References (30, 31)

8 July 2016; accepted 26 September 2016  
Published online 20 October 2016  
10.1126/science.aah4243

#### QUANTUM GASES

# Universal space-time scaling symmetry in the dynamics of bosons across a quantum phase transition

Logan W. Clark,\* Lei Feng, Cheng Chin

The dynamics of many-body systems spanning condensed matter, cosmology, and beyond are hypothesized to be universal when the systems cross continuous phase transitions. The universal dynamics are expected to satisfy a scaling symmetry of space and time with the crossing rate, inspired by the Kibble-Zurek mechanism. We test this symmetry based on Bose condensates in a shaken optical lattice. Shaking the lattice drives condensates across an effectively ferromagnetic quantum phase transition. After crossing the critical point, the condensates manifest delayed growth of spin fluctuations and develop antiferromagnetic spatial correlations resulting from the sub-Poisson distribution of the spacing between topological defects. The fluctuations and correlations are invariant in scaled space-time coordinates, in support of the scaling symmetry of quantum critical dynamics.

Critical phenomena near a continuous phase transition reveal fascinating connections between seemingly disparate systems that can be described via the same universal principles. Such systems can be found in the contexts of superfluid helium (1), liquid crystals (2), biological cell membranes (3), the early universe (4), and cold atoms (5, 6). An important universal prediction is the power-law scaling of the topological defect density with the rate of crossing a critical point, as first discussed by T. Kibble in cosmology (4) and extended by W. Zurek in the context of condensed matter (1). Their theory, known as the Kibble-Zurek mechanism, has been the subject of intense experimental study that has largely supported the scaling laws (7). Recent theoretical works further propose the so-called universality hypothesis, according to which the collective dynamics across a critical point should be invariant in the space and time coordinates that scale with the Kibble-Zurek power law (8–10).

Atomic quantum gases provide a clean, well-characterized, and controlled platform for studying critical dynamics (6, 11, 12). They have enabled experiments on the formation of topological defects

across the Bose-Einstein condensation transition (13–16) as well as critical dynamics across quantum phase transitions (17–23). Recent experiments using cold atoms in shaken optical lattices (24–26) have provided a vehicle for exploring phase transitions in spin models (27–29).

Here we study the critical dynamics of Bose condensates in a shaken optical lattice near an effectively ferromagnetic quantum phase transition. The transition occurs when we ramp the shaking amplitude across a critical value, causing the atomic population to bifurcate into two pseudo-spinor ground states (28). We measure the growth of spin fluctuations and the spatial spin correlations for ramping rates varied over two orders of magnitude. Beyond the critical point, we observe delayed development of ferromagnetic spin domains with long-range antiferromagnetic correlations due to the bunching of the domain sizes, which is not expected in a thermal distribution of ferromagnets. The times and lengths characterizing the critical dynamics agree with the scaling predicted by the Kibble-Zurek mechanism. The measured fluctuations and correlations collapse onto single curves in scaled space and time coordinates, supporting the universality hypothesis.

Our experiments use elongated three-dimensional (3D) Bose-Einstein condensates (BECs) of cesium atoms. We optically confine the condensates with trap frequencies of  $(\omega_x, \omega_y, \omega_z) = 2\pi \times (12, 30, 70)$

James Franck Institute, Enrico Fermi Institute and Department of Physics, University of Chicago, Chicago, IL 60637, USA.

\*Corresponding author. Email: lwclark@uchicago.edu

Hz, where the long ( $x'$ ) and short ( $y'$ ) axes are oriented at  $45^\circ$  with respect to the  $x$  and  $y$  coordinates (Fig. 1A). The tight confinement along the vertical  $z$  axis suppresses nontrivial dynamics in that direction (see the discussion on the dynamics in the  $y$  direction below), which is also the optical axis of our imaging system. We adiabatically load the condensates into a 1D optical lattice (1D) along the  $x$  axis with a lattice spacing of 532 nm and a depth of  $8.86 E_R$ , where  $E_R = \hbar \times 1.33$  kHz is the recoil energy and  $\hbar$  is Planck's constant.

To induce the ferromagnetic quantum phase transition, we modulate the phase of the lattice beam to periodically translate the lattice potential by  $\Delta x(t) = (s/2)\sin(\omega t)$ , where  $s$  is the shaking amplitude and the modulation frequency  $\omega$  is tuned to mix the ground and first excited lattice bands (fig. S1) (28, 30). The hybridized single-particle ground band energy  $\epsilon$  can be modeled for small quasimomentum  $\mathbf{q} = (q_x, q_y, q_z)$  by

$$\epsilon(\mathbf{q}; s) = \alpha(s)q_x^2 + \beta(s)q_x^4 + \frac{q_y^2 + q_z^2}{2m} \quad (1)$$

where  $m$  is the atomic mass, and the coefficients of its quadratic ( $\alpha$ ) and quartic ( $\beta$ ) terms depend on the shaking amplitude (Fig. 1B). For shaking amplitudes below the critical value, the coefficient  $\alpha$  is positive and the BEC occupies the lone ground state at momentum  $\mathbf{q} = 0$ . The quantum phase transition occurs when the quadratic term crosses zero at  $s = s_c$ , where  $\alpha = 0$  and  $\beta > 0$ . At this point, the speed of sound for superfluid excitations, formally studied in (31), drops to zero along  $x$  but remains nearly constant along  $y$  and  $z$ . Even stronger shaking converts the ground band into a double well with  $\alpha < 0$ , yielding two degenerate ground states with  $q_x = \pm q^*$ . Repulsively interacting bosons with this double-well ground band are effectively ferromagnetic, having two degenerate many-body ground states with all atoms either pseudo-spin up ( $q_x = q^*$ ) or down ( $q_x = -q^*$ ) (28). Notably, transitioning to one of these two ground states requires the system to spontaneously break the symmetry of its Hamiltonian. Describing the dynamics across the critical point presents a major challenge because of the divergence of the correlation length of quasimomentum and the relaxation time (critical slowing).

The Kibble-Zurek mechanism provides a powerful insight into quantum critical dynamics. According to this theory, when the time remaining to reach the critical point inevitably becomes shorter than the relaxation time, the system becomes effectively frozen (Fig. 1C). The system only unfreezes at a delay time  $t_{KZ}$  after passing the critical point, when relaxation becomes faster than the ramp. At this time, topological defects become visible, and the typical distance  $d_{KZ}$  between neighboring defects is proportional to the equilibrium correlation length. The Kibble-Zurek mechanism predicts that  $t_{KZ}$  and  $d_{KZ}$  depend on the quench rate  $\dot{s}$  as

$$t_{KZ} \propto \dot{s}^{-a}, \quad a = \frac{z\nu}{1+z\nu} \quad (2)$$

$$d_{KZ} \propto \dot{s}^{-b}, \quad b = \frac{\nu}{1+z\nu} \quad (3)$$

where  $z$  and  $\nu$  are the equilibrium dynamical and correlation length exponents given by the universality class of the phase transition. Although the details of this picture may not apply to every phase transition, the general scaling arguments are very robust, and similar predictions hold for a variety of quench types across the transition (12) and for phase transitions that break either continuous or discrete symmetries (7).

For slow ramps,  $t_{KZ}$  and  $d_{KZ}$  diverge and become separated from other scales in the system, making them the dominant scales for characterizing the collective critical dynamics (8–10). This idea motivates the universality hypothesis, which can be expressed as

$$f(x, t; \dot{s}) \propto F\left(\frac{x}{d_{KZ}}, \frac{t}{t_{KZ}}\right) \quad (4)$$

indicating that the critical dynamics of any collective observable  $f$  obeys the scaling symmetry and can be described by a universal function  $F$  of the scaled coordinates  $x/d_{KZ}$  and  $t/t_{KZ}$ . The only effect of the quench rate is to modify the length and time scales.

We test the scaling symmetry of time by monitoring the emergence of quasimomentum fluctuations at different quench rates. Here, fluctuations refer to deviations of quasimomentum from zero, which vary across space and between individual samples; fluctuations should saturate to a large value when domains having  $q = \pm q^*$  are fully formed. After loading the condensates into the lattice, we ramp the shaking amplitude linearly

from  $s = 0$  to values well above the critical amplitude  $s_c = 13.1$  nm (32) and interrupt the ramps at various times to perform a brief time-of-flight (TOF) before detection. After TOF, we measure the density deviation  $\delta n(\mathbf{r}) = n_{-1}(\mathbf{r}) - n_1(\mathbf{r}) - \langle n_{-1}(\mathbf{r}) - n_1(\mathbf{r}) \rangle$  (32), which is nearly proportional to the quasimomentum distribution (fig. S2), where  $n_i(\mathbf{r})$  is the density profile of the  $i$ th Bragg peak and the angle brackets denote averaging over multiple images. This detection method is particularly sensitive near the critical point when the quasimomentum just starts deviating from zero, indicating the emergence of fluctuations in the ferromagnetic phase where the ground states have nonzero quasimomentum. The spin density measurement used later to study spatial correlations is viable only when atoms settle to  $q = \pm q^*$ .

Over a wide range of quench rates, the evolution of quasimomentum fluctuation can be described in three phases (Fig. 2A). First, below the critical point, quasimomentum fluctuation does not exceed its baseline level. Second, just after passing the critical point, critical slowing keeps the system “frozen,” and fluctuation remains low. Finally, the system unfreezes and quasimomentum fluctuation quickly increases and saturates, indicating the emergence of ferromagnetic domains. We quantify this progression by investigating the fluctuation of contrast  $\Delta c = \langle \delta n^2 / n^2 \rangle$  (Fig. 2B) that tracks quasimomentum fluctuation in our condensates via the fluctuation of  $\delta n$  (fig. S2), where  $n$  is the total density and the angle brackets denote averaging over space and over multiple images. For comparison between different quench rates, we calculate the normalized fluctuation  $\Delta C = (\Delta c - \Delta c_i) / (\Delta c_f - \Delta c_i)$ , where

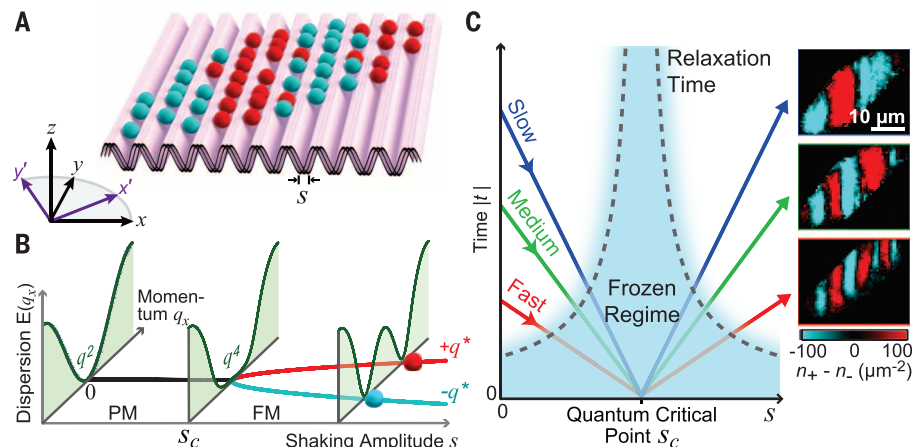


**Fig. 1. Ferromagnetic quantum phase transition of bosons in a shaken optical lattice.** (A) A BEC of cesium atoms (spheres) in a 1D optical lattice (pink surface) shaking with peak-to-peak amplitude  $s$  can form ferromagnetic domains (blue and red regions). The elliptical harmonic confinement has principal axes rotated  $45^\circ$  from the lattice. (B) The transition occurs when the ground band evolves from quadratic for  $s < s_c$  [paramagnetic (PM) phase], through quartic at the quantum critical point  $s = s_c$ , to a double well for  $s > s_c$  [ferromagnetic (FM) phase] with two minima at  $q_x = \pm q^*$  (28). (C) Kibble-Zurek picture. Evolution of the condensate crossing the phase transition becomes adiabatic in the frozen regime (cyan) when the time  $t$  remaining to reach the critical point is less than the relaxation time. Faster ramps cause freezing farther from the critical point, limiting the system to smaller domains. Sample domain images are shown for slow, medium, and fast ramps.

subscripts *i* and *f* indicate the fluctuation at early and late times, respectively (32). We find empirically that the growth of normalized fluctuations is well fit by the function

$$\Delta C(t) = \frac{1}{2} + \frac{1}{2} \tanh\left(\frac{t - t_d}{t_f}\right) \quad (5)$$

where the time *t* is defined relative to when the system crosses the critical point at *t* = 0, *t<sub>d</sub>* characterizes the delay time when the system unfreezes, and *t<sub>f</sub>* is the formation time over which the fluctuation grows. The measurement of fluctuation over time provides a critical test for both the Kibble-Zurek scaling and the universality hypothesis. First, both *t<sub>d</sub>* and *t<sub>f</sub>* exhibit clear power-law scaling with the quench rate  $\dot{s}$  varied over more than two orders of magnitude (Fig. 2C). Power-law fits yield the exponents of  $a_d = 0.50(2)$  and  $a_f = 0.50(6)$ , respectively. The nearly equal exponents are suggestive of the universality hypothesis, which requires all times to scale identically. Indeed, the growth of contrast fluctuation  $\Delta C$  follows a universal curve when time is scaled by *t<sub>d</sub>* (Fig. 2D), strongly supporting the universality hypothesis (Eq. 4). Note that any observable time characterizing the collective dynamics can be chosen as *t<sub>kz</sub>* in Eq. 4, including *t<sub>d</sub>* and *t<sub>f</sub>*.

We next test the spatial scaling symmetry based on the structures of pseudo-spin domains that emerge after the system unfreezes. Here, we cross the critical point with two different protocols: The first is a linear ramp starting from *s* = 0, whereas the second begins with a jump to *s* = *s<sub>c</sub>*, followed by a linear ramp. We detect domains near the time *t* = 1.4*t<sub>d</sub>* in the spin density distribution  $j_z(\mathbf{r}) = n_+(\mathbf{r}) - n_-(\mathbf{r})$  based on the density *n<sub>+/-</sub>* of atoms with spin up/down (fig. S3). At this time, the spin domains are fully formed and clearly separated by topological defects (domain walls), as shown in Fig. 3A. Furthermore, choosing this time just after domain formation minimizes the time available for nonuniversal relaxation processes. We characterize the domain distribution with the spin correlation function (17, 28)

$$G(\mathbf{r}) = \left\langle \int j_z(\mathbf{R} + \mathbf{r}) j_z(\mathbf{R}) d\mathbf{R} \right\rangle \quad (6)$$

averaged over multiple images (Fig. 3B). Both ramping protocols lead to similar correlation functions, suggesting that the domain distribution is insensitive to increases in the quench rate below the critical point.

The spin correlations reveal rich domain structure that strongly depends on the quench rate. For slower ramps  $\dot{s} < 1.3$  nm/ms, the structures are predominantly one-dimensional and the density of topological defects increases with the quench rate. The tighter confinement and finite speed of sound near the critical point along the *y* and *z* axes allow spin correlations to span the gas in those directions. The dynamics thus appear one-dimensional. When the quench rate exceeds 1.3 nm/ms, defects start appearing along the *y* axis, and the domain structures become multidimensional. We attribute this dimensional crossover to the unfreezing

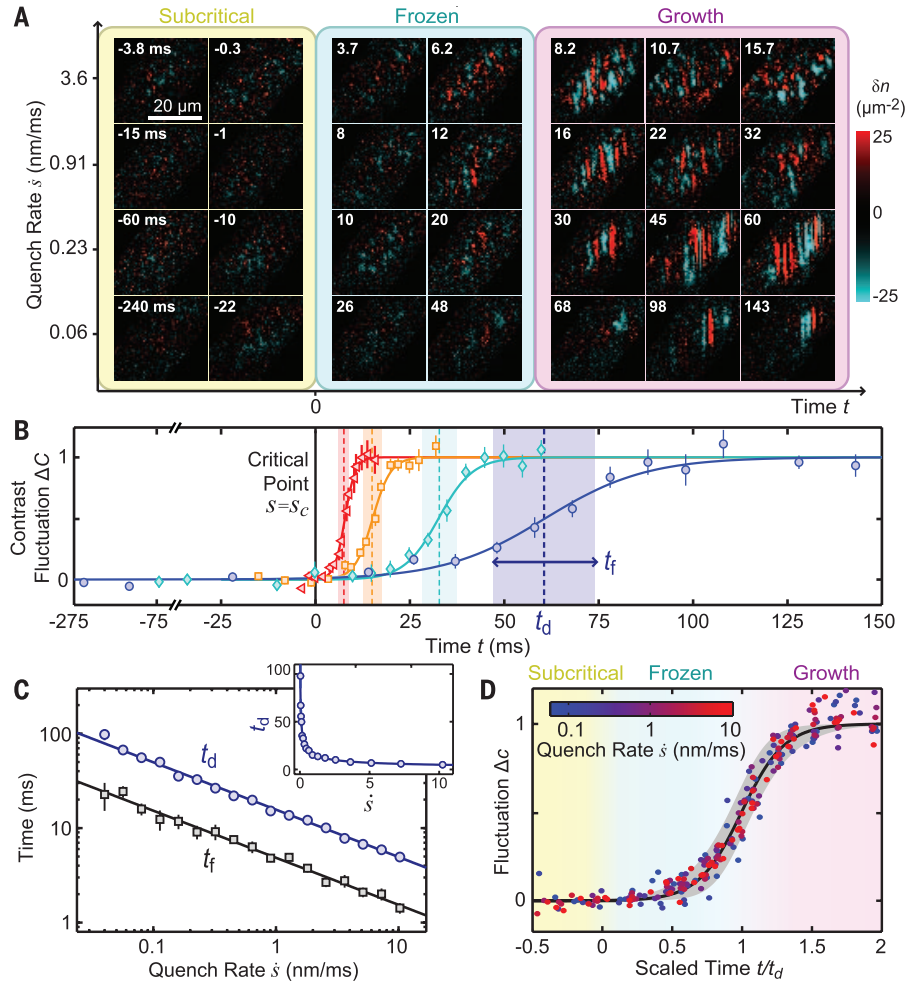


**Fig. 2. Growth of quasimomentum fluctuation in quantum critical dynamics.** (A) Sample images show the emergence of nonzero local quasimomentum via the density deviation between Bragg peaks  $\delta n$  as the system is linearly ramped across the ferromagnetic phase transition; four ramps with increasing quench rates (bottom to top) are shown. Each ramp exhibits three regimes: a subcritical regime before the transition; a frozen regime beyond the critical point where the fluctuation remains low; and a growth regime in which fluctuation increases and saturates, indicating domain formation. Time *t* = 0 corresponds to the moment when the system reaches the critical point. (B) Quasimomentum fluctuation for ramp rates  $\dot{s} = 3.6$  (triangles), 0.91 (squares), 0.23 (diamonds), and 0.06 nm/ms (circles) arises at a delay time *t* = *t<sub>d</sub>* over a formation time *t<sub>f</sub>*. Fluctuation is normalized for each ramp rate to aid comparison (32). The solid curves show fits based on Eq. 5. (C) The dependence of *t<sub>d</sub>* (circles) and *t<sub>f</sub>* (squares) on the quench rate is well fit by power laws (solid curves) with scaling exponents of  $a_d = 0.50(2)$  and  $a_f = 0.50(6)$ , respectively. The inset shows *t<sub>d</sub>* on a linear scale. (D) Fluctuations measured for 16 ramp rates from 0.06 to 10.3 nm/ms collapse to a single curve when time is scaled by *t<sub>d</sub>* based on the power-law fit. The solid curve shows the best fit based on the empirical function (Eq. 5), and the gray shaded region covers one standard deviation. Error bars in (B) and (C) indicate one standard error.

time becoming too short to establish correlation along the *y* axis. For the remainder of this work, we focus on the slower quenches and investigate the spin correlations along the *x* axis.

We examine the 1D correlations using line cuts of the density-weighted correlation functions  $g(\mathbf{r}) = G(\mathbf{r}) / \langle n(\mathbf{R} + \mathbf{r}) n(\mathbf{R}) \rangle$  (17, 28). The results exhibit prominent decaying oscillation (Fig. 3C). We extract two essential length scales from the correlation functions: the average domain size *d*, or equivalently, the distance between neighboring topological defects, and the correlation length  $\xi$ , indicating the width of the envelope function.

These two scales are determined from the position and width of the peak in the Fourier transform of  $g(x)$  (32).

These length scales enable us to test the spatial scaling symmetry. The lengths *d* and  $\xi$  both display power-law scaling consistent with the Kibble-Zurek mechanism (Fig. 3D), with fits yielding exponents  $b_d = 0.26(2)$  for the domain size and  $b_\xi = 0.26(5)$  for the correlation length. Similarly, the correlations, measured at the same scaled time, collapse to a single curve in spatial coordinates scaled by the domain size *d* (Fig. 3E). This result strongly supports the spatiotemporal scaling from

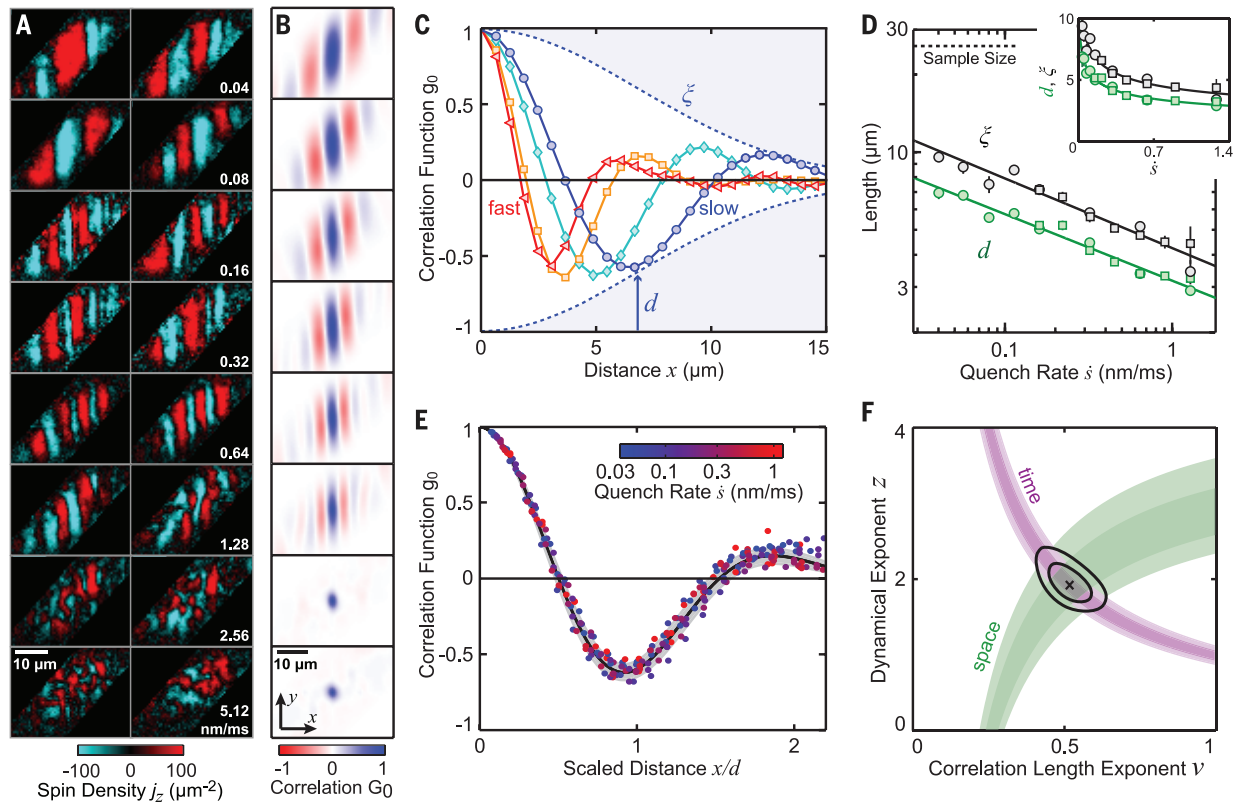


**Fig. 3. Antiferromagnetic spatial correlations from quantum critical dynamics.** (A) Two sample images at each quench rate exemplify spin domains measured near the time  $t = 1.4t_d$  after crossing the phase transition. These images correspond to linear ramps starting at  $s = 0$  ( $s = 0.32$  to  $5.12$  nm/ms) and  $s = s_c$  ( $s = 0.04$  to  $0.16$  nm/ms). (B) Spin correlation functions  $G_0(\mathbf{r}) = G(\mathbf{r})/G(0)$  (Eq. 6) are calculated from ensembles of 110 to 200 images. (C) Cuts across the density-weighted correlation functions  $g_0(x) = g(x)/g(0)$  are shown for quench rates  $\dot{s} = 1.28$  (triangles),  $0.45$  (squares),  $0.16$  (diamonds), and  $0.056$  nm/ms (circles). Solid curves interpolate the data to guide the eye. The typical domain size  $d$  and the correlation length  $\xi$  are illustrated for  $0.056$  nm/ms by the arrow and dashed envelope, respectively (32). (D) The dependence of

$d$  (green) and  $\xi$  (black) on the quench rate is well fit by power laws (Eq. 3) with spatial scaling exponents of  $b_d = 0.26(2)$  and  $b_\xi = 0.26(5)$ , respectively. Marker shape indicates linear ramps starting at  $s = 0$  (squares) or at  $s = s_c$  (circles). The inset shows the results on a linear scale. Error bars indicate 1 SE. (E) Correlation functions for  $\dot{s} = 0.04$  to  $1.28$  nm/ms collapse to a single curve when distance is scaled by the domain size extracted from the power-law fit in (D). The solid curve shows the fit based on Eq. 7; the gray shaded area covers 1 SD. (F) The temporal scaling exponents  $a_d$  and  $a_\xi$  from Fig. 2C (magenta) and the spatial scaling exponents  $b_d$  and  $b_\xi$  from (D) (green) constrain the critical exponents  $\nu$  and  $z$  according to Eqs. 2 and 3 with 68% (dark) and 95% (light) confidence intervals. The cross marks the best values with contours of 68 and 95% overall confidence (32).

the universality hypothesis (Eq. 4). An empirical curve

$$g_0(x) = \exp\left(-\frac{1}{2\sigma^2} \frac{x^2}{d^2}\right) \cos\left(\frac{\pi x}{\gamma d}\right) \quad (7)$$

provides a good fit to the universal correlation function, yielding  $\sigma = 1.01(1)$  and  $\gamma = 1.04(1)$ , indicating that the width of the envelope is close to the typical domain size.

The most striking feature of the universal correlation function is the emergence of oscillatory, antiferromagnetic order in the ferromagnetic phase. In thermal equilibrium, ferromagnets are expected to have a finite correlation length but no anticorrelation. The appearance of strong anticorrelation at  $x = d$  suggests that domains of size  $d$  form preferentially during the quantum critical dynamics. A statistical analysis of the topological defect distribution reveals that the domain sizes are bunched with their standard deviation  $\sigma_d = 0.31(2)d$  well below their mean, indicating that the topological defects are created by a sub-Poisson process (fig. S4).

Finally, the combined scaling exponents of space and time allow us to extract the equilibrium critical exponents based on the Kibble-Zurek mechanism (33) (Fig. 3F). Solving Eqs. 2 and 3, we obtain the dynamical exponent  $z = 1.9(2)$  and correlation length exponent  $\nu = 0.52(5)$ , which are close to the mean-field values  $z = 2$  and  $\nu = 1/2$  up to our experimental uncertainty. Note that the dynamical critical exponent  $z = 2$  results from the unique quartic kinetic energy  $\varepsilon = \beta q_x^4$  of our system at the critical point (32).

Direct identification of domain walls presents intriguing possibilities for future studies of the topological defects generated during critical dynamics. These opportunities would be particularly interesting if the shaking technique were extended to higher dimensions in such a way that the transition breaks a continuous symmetry. In addition, the scaling of the correlation functions suggests that the antiferromagnetic order may be a shared feature of quantum critical dynamics for phase transitions in the same universality class, meriting future experiments.

#### REFERENCES AND NOTES

- W. H. Zurek, *Nature* **317**, 505–508 (1985).
- I. Chuang, R. Durrer, N. Turok, B. Yurke, *Science* **251**, 1336–1342 (1991).
- S. L. Veatch, O. Soubias, S. L. Keller, K. Gawrisch, *Proc. Natl. Acad. Sci. U.S.A.* **104**, 17650–17655 (2007).
- T. W. B. Kibble, *J. Phys. Math. Gen.* **9**, 1387–1398 (1976).
- Q. Zhou, T. L. Ho, *Phys. Rev. Lett.* **105**, 245702 (2010).
- A. Polkovnikov, K. Sengupta, A. Silva, M. Vengalattore, *Rev. Mod. Phys.* **83**, 863–883 (2011).
- A. del Campo, W. H. Zurek, *Int. J. Mod. Phys. A* **29**, 1430018 (2014).
- M. Kolodrubetz, B. K. Clark, D. A. Huse, *Phys. Rev. Lett.* **109**, 015701 (2012).
- A. Chandran, A. Erez, S. S. Gubser, S. L. Sondhi, *Phys. Rev. B* **86**, 064304 (2012).
- A. Francuz, J. Dziarmaga, B. Gardas, W. H. Zurek, *Phys. Rev. B* **93**, 075134 (2016).
- I. Bloch, J. Dalibard, W. Zwerger, *Rev. Mod. Phys.* **80**, 885–964 (2008).
- J. Dziarmaga, *Adv. Phys.* **59**, 1063–1189 (2010).
- C. N. Weiler *et al.*, *Nature* **455**, 948–951 (2008).
- G. Lamporesi, S. Donadello, S. Serafini, F. Dalfovo, G. Ferrari, *Nat. Phys.* **9**, 656–660 (2013).
- L. Cormran *et al.*, *Phys. Rev. Lett.* **113**, 135302 (2014).
- N. Navon, A. L. Gaunt, R. P. Smith, Z. Hadzibabic, *Science* **347**, 167–170 (2015).
- L. E. Sadler, J. M. Higbie, S. R. Leslie, M. Vengalattore, D. M. Stamper-Kurn, *Nature* **443**, 312–315 (2006).

18. K. Baumann, R. Mottl, F. Brennecke, T. Esslinger, *Phys. Rev. Lett.* **107**, 140402 (2011).
19. D. Chen, M. White, C. Borries, B. DeMarco, *Phys. Rev. Lett.* **106**, 235304 (2011).
20. E. Nicklas *et al.*, *Phys. Rev. Lett.* **115**, 245301 (2015).
21. S. Braun *et al.*, *Proc. Natl. Acad. Sci. U.S.A.* **112**, 3641–3646 (2015).
22. C. Meldgin *et al.*, *Nat. Phys.* **12**, 646–649 (2016).
23. M. Anquez *et al.*, *Phys. Rev. Lett.* **116**, 155301 (2016).
24. N. Gemelke, E. Sarajlic, Y. Bidel, S. Hong, S. Chu, *Phys. Rev. Lett.* **95**, 170404 (2005).
25. H. Lignier *et al.*, *Phys. Rev. Lett.* **99**, 220403 (2007).
26. J. Struck *et al.*, *Phys. Rev. Lett.* **108**, 225304 (2012).
27. J. Struck *et al.*, *Science* **333**, 996–999 (2011).
28. C. V. Parker, L.-C. Ha, C. Chin, *Nat. Phys.* **9**, 769–774 (2013).
29. G. Jotzu *et al.*, *Nature* **515**, 237–240 (2014).
30. W. Zheng, B. Liu, J. Miao, C. Chin, H. Zhai, *Phys. Rev. Lett.* **113**, 155303 (2014).
31. L.-C. Ha, L. W. Clark, C. V. Parker, B. M. Anderson, C. Chin, *Phys. Rev. Lett.* **114**, 055301 (2015).
32. Materials and methods are available on Science Online.
33. J. Xu *et al.*, *Europhys. Lett.* **113**, 50003 (2016).

## ACKNOWLEDGMENTS

We thank L.-C. Ha, C. V. Parker, B. M. Anderson, B. J. DeSalvo, A. Polkovnikov, S. Sachdev, and Q. Zhou for helpful discussions. L.W.C. was supported by a National Defense Science and

Engineering Graduate Fellowship and a Nambu Fellowship. This work was supported by NSF Materials Research Science and Engineering Centers (DMR-1420709), NSF grant PHY-1511696, and Army Research Office–Multidisciplinary Research Initiative grant W911NF-14-1-0003. The data presented in this paper are available upon request to C.C. (cchin@uchicago.edu).

## SUPPLEMENTARY MATERIALS

www.sciencemag.org/content/354/6312/606/suppl/DC1  
Materials and Methods  
Figs. S1 to S4  
References (34, 35)

28 April 2016; accepted 26 September 2016  
10.1126/science.aaf9657

## PHYSICS

# Buffer-gas cooling of antiprotonic helium to 1.5 to 1.7 K, and antiproton-to-electron mass ratio

Masaki Hori,<sup>1\*</sup> Hossein Aghai-Khozani,<sup>1</sup> Anna Sótér,<sup>1</sup> Daniel Barna,<sup>2</sup> Andreas Dax,<sup>3†</sup> Ryugo Hayano,<sup>3</sup> Takumi Kobayashi,<sup>3‡</sup> Yohei Murakami,<sup>3</sup> Koichi Todoroki,<sup>3§</sup> Hiroyuki Yamada,<sup>3</sup> Dezső Horváth,<sup>2,4</sup> Luca Venturelli<sup>5</sup>

Charge, parity, and time reversal (CPT) symmetry implies that a particle and its antiparticle have the same mass. The antiproton-to-electron mass ratio  $M_{\bar{p}}/m_e$  can be precisely determined from the single-photon transition frequencies of antiprotonic helium. We measured 13 such frequencies with laser spectroscopy to a fractional precision of  $2.5 \times 10^{-9}$  to  $16 \times 10^{-9}$ . About  $2 \times 10^9$  antiprotonic helium atoms were cooled to temperatures between 1.5 and 1.7 kelvin by using buffer-gas cooling in cryogenic low-pressure helium gas; the narrow thermal distribution led to the observation of sharp spectral lines of small thermal Doppler width. The deviation between the experimental frequencies and the results of three-body quantum electrodynamics calculations was reduced by a factor of 1.4 to 10 compared with previous single-photon experiments. From this,  $M_{\bar{p}}/m_e$  was determined as  $1836.1526734(15)$ , which agrees with a recent proton-to-electron experimental value within  $8 \times 10^{-10}$ .

Techniques to cool atoms containing antiparticles such as antihydrogen (1, 2), positronium (3, 4), or antiprotonic helium ( $\bar{p}\text{He}^+$ ) (5, 6) allow their spectral lines to be measured with narrow thermal Doppler widths and strong signal intensities. Their transition frequencies can then be determined with the highest precision, thus increasing the sensitivity of the experiments to the consistency of charge, parity, and time reversal (CPT) symmetry (7), which implies that particles and antiparticles have equal

masses and absolute values of the charge. Spectral data on  $\bar{p}\text{He}^+$  have also been used to set upper limits on a possible fifth force at angstrom-length scales (8, 9). Buffer-gas cooling techniques (10, 11) have been used to cool many ordinary atoms and molecules that lack the closed-cycle transitions suitable for laser cooling. It relies on elastic collisions between the atom of interest with a cryogenic buffer gas to allow the system to reach thermal equilibrium. Here, we report on the application of this method to cool large ( $2 \times 10^9$ ) numbers of  $\bar{p}^1\text{He}^+$  and  $\bar{p}^3\text{He}^+$  isotopes to temperatures  $T = 1.5$  to 1.7 K.

Metastable  $\bar{p}\text{He}^+$  is a three-body exotic atom (fig. S1) that contains a helium nucleus, an electron occupying the 1s state, and an antiproton in a Rydberg state of principal- and angular-momentum quantum numbers  $n \sim l + 1 \sim 38$  (5, 12–15). The antiproton that occupies these circular orbitals that lie  $\sim 80$  keV above the 1s antiprotonic state retains microsecond-scale lifetimes against annihilation in the nucleus because it is localized away from the nucleus. Before this experiment, it was not known whether collisions with normal-

matter atoms would cool  $\bar{p}\text{He}^+$  to such low (1.5 K) temperatures because the corresponding multi-body calculations were complicated. In fact, other exotic atoms such as pionic hydrogen (16) were heated by collisions that deexcite the atom;  $\bar{p}\text{He}^+$  atoms colliding with other helium atoms annihilated (5) the antiprotons occupying some states. We adjusted the density of the buffer helium gas so that the  $\bar{p}\text{He}^+$  atoms, once formed, rapidly underwent a few hundred or more cooling collisions before being interrogated by the laser beam. The 1s electron protected most of the  $\bar{p}\text{He}^+$  atoms during this cooling.

The  $\bar{p}\text{He}^+$  transition frequencies have recently been calculated (12–15) to a precision of  $\sim 10^{-10}$  by evaluating the complete set of quantum electrodynamics (QED) corrections up to order  $m_e\alpha^7$  in atomic units. These a priori calculations used the International Council for Science Committee on Data for Science and Technology (CODATA) 2010–recommended values of the fundamental constants (17), including the fine structure constant  $\alpha$ , the  $^3\text{He}$ - and  $^4\text{He}$ -to-electron mass ratios, the Bohr radius, and the Rydberg constant. By comparing the calculated and experimental  $\bar{p}\text{He}^+$  frequencies, the  $M_{\bar{p}}/m_e$  ratio can in principle be determined to a fractional precision of  $<1 \times 10^{-10}$  (12–15), which may rival the best measurements of the proton-to-electron mass ratio  $M_p/m_e$  (18–22). Previous measurements (23) of the  $\bar{p}\text{He}^+$  single-photon frequencies, however, differed by up to  $8 \times 10^{-8}$  from the calculations available at the time, which corresponded in some cases to 2 to 3 standard experimental deviations. A major source of experimental uncertainty was the Doppler broadening of the spectral lines. We later measured a different set of two-photon resonances using a Doppler-cancellation technique (6) in which  $\bar{p}\text{He}^+$  atoms were irradiated by a pair of counterpropagating laser beams. Three transition frequencies involving the  $n < 36$  states were measured with this complicated method. Assuming CPT invariance, the results were included in the CODATA2010 data set in order to determine the electron mass  $m_e$  in atomic mass units; however, further improvements in the precision of the determination of  $M_{\bar{p}}/m_e$  were limited by the poor experimental precision of the single-photon frequencies (23) that had higher sensitivities  $\kappa_M$  (5) to  $M_{\bar{p}}/m_e$  and  $m_e$ , as compared with those of the two-photon lines (Table 1). The Doppler-broadened single-photon

<sup>1</sup>Max-Planck-Institut für Quantenoptik, Hans-Kopfermann-Strasse 1, 85748 Garching, Germany. <sup>2</sup>MTA Wigner Research Centre for Physics, H-1525 Budapest, Hungary. <sup>3</sup>Department of Physics, University of Tokyo, Hongo, Bunkyo-ku, Tokyo 113-0033, Japan. <sup>4</sup>Institute of Nuclear Research (ATOMKI), H-4001 Debrecen, Hungary. <sup>5</sup>Dipartimento di Ingegneria dell'Informazione, Università di Brescia, Istituto Nazionale di Fisica Nucleare, I-25133 Brescia, Italy.

\*Corresponding author. Email: masaki.hori@mpq.mpg.de

†Present address: Paul Scherrer Institut, CH-5232 Villigen, Switzerland. ‡Present address: National Metrology Institute of Japan (NMIJ), National Institute of Advanced Industrial Science and Technology (AIST), 1-1-1 Umezono, Tsukuba, Ibaraki 305-8563, Japan. §Present address: NEC Corporation, Shiba, Minato-Ku, Tokyo, Japan.

EXTENDED PDF FORMAT  
SPONSORED BY



**Universal space-time scaling symmetry in the dynamics of bosons across a quantum phase transition**

Logan W. Clark, Lei Feng and Cheng Chin (November 3, 2016)  
*Science* **354** (6312), 606-610. [doi: 10.1126/science.aaf9657]

Editor's Summary

**Shaking the lattice uncovers universality**

Most of our knowledge of quantum phase transitions (QPTs)—which occur as a result of quantum, rather than thermal, fluctuations—comes from experiments performed in equilibrium conditions. Less is known about the dynamics of a system going through a QPT, which have been hypothesized to depend on a single time and length scale. Clark *et al.* confirmed this hypothesis in a gas of cesium atoms in an optical lattice, which was shaken progressively faster to drive the gas through a QPT.

*Science*, this issue p. 606

---

This copy is for your personal, non-commercial use only.

---

- Article Tools** Visit the online version of this article to access the personalization and article tools:  
<http://science.sciencemag.org/content/354/6312/606>
- Permissions** Obtain information about reproducing this article:  
<http://www.sciencemag.org/about/permissions.dtl>

*Science* (print ISSN 0036-8075; online ISSN 1095-9203) is published weekly, except the last week in December, by the American Association for the Advancement of Science, 1200 New York Avenue NW, Washington, DC 20005. Copyright 2016 by the American Association for the Advancement of Science; all rights reserved. The title *Science* is a registered trademark of AAAS.



www.sciencemag.org/content/354/6312/606/suppl/DC1

## Supplementary Materials for

### **Universal space-time scaling symmetry in the dynamics of bosons across a quantum phase transition**

Logan W. Clark,\* Lei Feng, Cheng Chin

\*Corresponding author. Email: lwclark@uchicago.edu

Published 4 November 2016, *Science* **354**, 606 (2016)  
DOI: 10.1126/science.aaf9657

#### **This PDF file includes:**

Materials and Methods  
Figs. S1 to S4  
References

## Materials and Methods

### Experiment Setup

Our condensates form in an optical dipole trap at the crossing of three lasers with wavelength  $\lambda = 1064$  nm. After evaporation the condensates are nearly pure, consisting of 30 000 to 40 000 atoms with temperatures less than 10 nK. We adiabatically load the condensates into an optical lattice by retro-reflecting the trapping beam along the  $x$ -axis. The apparatus which enables us to shake the lattice is described in Ref. (28).

Our experiments rely on a careful choice of the parameters governing the shaking optical lattice. We set the shaking frequency  $\omega = 2\pi \times 8.00$  kHz slightly above the zero-momentum band gap  $h \times 7.14$  kHz, such that shaking raises the energy near the center of the ground band. During shaking we reduce the scattering length to  $a = 2.1$  nm using a Feshbach resonance to lower the heating rate (34). Finally, immediately before time-of-flight (TOF) we reduce the scattering length to  $a = 0$  to prevent collisions while the atoms separate into distinct Bragg peaks.

Based on the lattice depth and shaking frequency, we calculate the critical shaking amplitude  $s_c = 13.1$  nm using Floquet theory (28), above which the system acquires a double-well ground band (see Fig. S1A&B). We base our calculation of  $a_d = 0.50(2)$  on this theoretical critical point. To verify the critical value  $s_c = 13.1$  nm, we allow the critical shaking amplitude to be a free parameter in a power law fit of  $t_d$  while fixing the exponent to its theoretical value of 0.5. The fit yields  $s_c = 13.8(6)$  nm which is consistent with the calculated critical amplitude. From the Floquet theory we also calculate the quasimomentum at the double-well minima, which follows  $q^* = \gamma(s - s_c)^{1/2}$  near the critical point with  $\gamma = h \times 2.0 \mu\text{m}^{-3/2}$  (see Fig. S1C). Using the power-law fits from Fig. 2C & 3D, we find that the wavelength  $h/q^*$  at  $t = 1.4 t_d$  is quite close to the typical domain size  $d$ , with  $dq^*/h \approx 0.96(7)$ .

### Analysis of Quasimomentum Fluctuation

We use the density fluctuation in the Bragg peaks to detect quasimomentum fluctuation in the gas. Non-zero local quasimomentum  $q$  changes the local density difference between Bragg peaks. To detect this change we perform a brief TOF with duration  $t_{\text{TOF}} = 5$  ms, which is long enough to separate the Bragg peaks but short enough that spatial information is preserved. From our images we calculate the density difference  $\Delta n(\mathbf{r}) = n_{-1}(\mathbf{r}) - n_1(\mathbf{r})$  where  $n_i(\mathbf{r})$  is the density of the  $i$ 'th Bragg peak. To remove the small offset in  $\Delta n$  which exists at momentum  $q = 0$ , we calculate the density deviation  $\delta n(\mathbf{r}) = \Delta n(\mathbf{r}) - \langle \Delta n(\mathbf{r}) \rangle$ , where the angle brackets denote averaging over multiple images. The shift  $\delta n$  is nearly proportional to the local quasimomentum regardless of the shaking amplitude (Fig. S2). Finally, we calculate the contrast fluctuation  $\Delta c = \langle \delta n^2 / n^2 \rangle$  which closely tracks quasimomentum fluctuation in our condensates, where  $n(r)$  is the total density. The angle brackets denote averaging over many images and over the position within each sample.

In order to remove spurious sources of fluctuation such as photon and atom shot noise, we calculate the normalized fluctuations  $\Delta C = (\Delta c - \Delta c_i) / (\Delta c_f - \Delta c_i)$ . Here we subtract the baseline value  $\Delta c_i$  for each ramp rate, which is given by the average of the three measurements

at the earliest times taken below the critical point. Furthermore, even though quasimomentum fluctuation should continue to grow as  $q^{*2}$  with increasing shaking amplitude, where  $\pm q^*$  are the quasimomenta of the ground states, we find that  $\Delta c$  appears to saturate to a nearly constant value for times well beyond  $t_d$ . We attribute saturation to the typical displacement  $q^* t_{\text{TOF}}/m$  during TOF becoming larger than the correlation length, such that fluctuation is dominated by the motion rather than the density of the Bragg peaks. We normalize  $\Delta c$  to its saturated value  $\Delta c_f$  at each ramp rate for convenient comparison. We determine  $\Delta c_f$  by averaging the latest three measured values, which are taken well beyond the delay time  $t_d$ .

### Reconstruction of Pseudo-spin Domains

Reconstruction enables us to study the *in-situ* spin density distribution, including the domain structure. A previous study demonstrated that local variations in the distribution of density among the Bragg peaks after a short TOF could be used to reconstruct the pseudo-spin domains (28). In the present work at  $t = 1.4t_d$ , we observe density distributions after TOF consistent with nearly all atoms arranging into domains with  $q = \pm q^*$ , enabling us to treat them as pseudo-spins and calculate the spin density just after the system unfreezes.

We improve the domain reconstruction scheme described in Ref. (28) by adding an amplification stage before TOF. After linearly ramping the shaking amplitude at ramp rate  $\dot{s}$  until  $t = 1.4 t_d$  when domains have fully formed, we rapidly increase the shaking amplitude by as much as a factor of 15 over only 0.5 ms (Fig. S3A). The rapid increase in shaking amplitude excites the atoms to higher bands while leaving their quasimomentum approximately the same. For a proper choice of the shaking amplitude and timing during this amplification stage, the atoms are efficiently transferred to the second excited band before they are released for TOF. In the second excited band, pseudo-spin down atoms ( $q = -q^*$ ) will mostly appear in the  $-1$  Bragg peak while pseudo-spin up atoms ( $q = +q^*$ ) will mostly appear in the  $+1$  Bragg peak, making them easy to distinguish after the short TOF. Depending on the shaking amplitude at  $t = 1.4 t_d$ , we adjust the timing and the shaking amplitude immediately before release in order to maximize the distinguishability of the two spin states. We use images of condensates with uniform spin (Fig. S3B) to calibrate the projection of each spin state onto Bragg peaks (Fig. S3C). In comparison to the procedure without enhanced shaking used in Ref. (28), the amplification stage improves the fraction of atoms which distinguish the spin states from 23% to about 71%, corresponding to an increase in signal by more than a factor of three. After the enhanced shaking period, we perform a 3 ms TOF and measure the density in each Bragg peak (Fig. S3D), from which we can reconstruct the spin density distribution (Fig. S3E) using an algorithm similar to that described in Ref. (28).

### Minimizing bias of the total polarization

The effectively ferromagnetic quantum phase transition can be biased by a nonzero initial velocity of the condensate relative to the lattice (28). In order to focus our study on the dynamics across an unbiased quantum phase transition, we test the total spin polarization  $P = \int j_z(\vec{R})d\vec{R} / \int n(\vec{R})d\vec{R}$  of each reconstructed image, which is expected to be close to zero for unbiased samples. Indeed, under most conditions ( $0.16 \leq \dot{s} < 1.0$  nm/ms) we find that more

than 90% of images have total polarization  $|P| < 0.3$ . The correlation analysis excludes the remaining biased images with  $|P| > 0.3$ . For very slow ramps ( $\dot{s} < 0.16$  nm/ms) starting from  $s = 0$ , we find that many samples are biased, likely due to increased susceptibility to a small, uncontrolled velocity between the condensate and the lattice. We have excluded data from these conditions to avoid poor statistics.

### Removing systematic effects due to finite imaging resolution

We study the one-dimensional domain structures along the lattice direction ( $x$ ) by taking cuts  $g_{\text{meas}}(x)$  along the long-axis of the measured, normalized correlation functions  $g(\mathbf{r})$ . Since the domain walls are predominantly oriented along the non-lattice direction ( $y$ ), long axis cuts maximize the range of the correlation functions that we can evaluate but still reflect the structure along the lattice direction.

To obtain the physical spin correlations we must remove the systematic effects of our finite imaging resolution. Since the correlation functions depend on the spin density at both ends of the displacement vector, the measured correlations  $g_{\text{meas}}(x)$  are the physical correlations  $g(x)$  convolved with the point spread function  $P(x)$  twice (35). We calculate the Fourier transform of the deconvolved correlation function  $\tilde{g}(k) = \tilde{g}_{\text{meas}}(k)/\tilde{P}^2(k)$  from the Fourier transforms of the measured correlations  $\tilde{g}_{\text{meas}}(k)$  and of the point spread function  $\tilde{P}(k)$ . Inverting the Fourier transform produces the correlation functions  $g(x)$  shown in Fig. 3C. Furthermore, from the peak position  $k_p$  in  $\tilde{g}(k)$  we extract the typical domain size  $d = \pi/k_p$ , and from the full width at half maximum  $\Delta k$  of the peak we extract the correlation length  $\xi = \pi/\Delta k$ .

### Sub-Poisson generation of domain walls

To better understand the process which generates domain walls we calculate the domain size distribution from our images. We identify domain walls by integrating the spin density along the  $y$ -direction, filtering noise at the single pixel scale ( $0.6 \mu\text{m}$ ) which is below our resolution limit, and locating where the spin density changes sign. We calculate the domain sizes from the distances between neighboring walls.

Since the correlation functions in scaled space are invariant with quench rate we focus on a single rate  $\dot{s} = 0.08$  nm/ms, for which the domains are relatively large ( $d = 6.0 \mu\text{m}$ ) and easy to resolve. The resulting domain size distribution (Fig. S4A) is tightly bunched around its mean. This bunching would not be expected for a Poisson process, which should exhibit an exponential distribution due to the constant probability of forming a domain wall at any location. Similarly, Poisson generation of domain walls would lead to exponentially decaying correlations that are qualitatively distinct from the oscillatory correlations observed in our experiments (Fig. S4B).

### Equilibrium critical exponents $\nu$ and $z$

The partition function  $Z$  of our system near the critical point where  $\alpha \rightarrow 0$  and  $\beta > 0$  can be written in the path integral form as (30)

$$Z = \int D\Psi D\Psi^* e^{-\int dx d\tau L}$$

$$L = \Psi^* \partial_\tau \Psi + \alpha |\partial_x \Psi|^2 + \beta |\partial_x^2 \Psi|^2 - \mu \Psi^* \Psi + \frac{g}{2} (\Psi^* \Psi)^2,$$

where  $L$  is the mean field Lagrangian density,  $\mu = g\rho_0$  is the chemical potential,  $g$  is the interaction parameter and  $\tau = it/\hbar$ .

Given a fluctuating order parameter  $\Psi = \sqrt{\rho} e^{i\theta}$  around the equilibrium value  $\Psi_0 = \sqrt{\rho_0}$  and  $\rho = \rho_0 + \tilde{\rho}$ , we have

$$\begin{aligned} \Psi^* \partial_\tau \Psi &= i\rho \partial_\tau \theta + \partial_\tau \rho / 2 \\ |\partial_x \Psi|^2 &= \rho (\partial_x \rho)^2 + \frac{1}{4\rho} (\partial_x \theta)^2 \\ |\partial_x^2 \Psi|^2 &= \rho^{-3} \left( \frac{(\partial_x \rho)^2}{4} - \frac{\rho \partial_x^2 \rho}{2} + \rho^2 (\partial_x \theta)^2 \right)^2 + \rho^{-1} (\rho \partial_x^2 \theta - \partial_x \theta \partial_x \rho)^2 \\ -\mu \Psi^* \Psi + \frac{g}{2} (\Psi^* \Psi)^2 &= \frac{g}{2} (\tilde{\rho}^2 - \rho_0^2). \end{aligned}$$

Eliminating terms like  $\partial_\tau \rho$  and  $\rho_0 \partial_\tau \theta$  that contribute to constants after integration over  $\tau$ , we have

$$\begin{aligned} L = i\tilde{\rho} \partial_\tau \theta + \frac{\alpha}{\rho} \left( \rho^2 (\partial_x \rho)^2 + \frac{(\partial_x \theta)^2}{4} \right) \\ + \frac{\beta}{\rho^3} \left( \frac{(\partial_x \tilde{\rho})^2}{4} - \frac{\rho \partial_x^2 \tilde{\rho}}{2} + \rho^2 (\partial_x \theta)^2 \right)^2 + \frac{\beta}{\rho} (\rho \partial_x^2 \theta - \partial_x \theta \partial_x \tilde{\rho})^2 + \frac{g}{2} \tilde{\rho}^2. \end{aligned}$$

Since the amplitude excitations are gapped and the angular excitations are gapless, we can assume  $\partial_x \tilde{\rho} = 0$  in the long wavelength limit, which gives

$$L = i\tilde{\rho} \partial_\tau \theta + \alpha \rho \frac{(\partial_x \theta)^2}{4} + \beta \rho (\partial_x \theta)^2 + \beta \rho (\partial_x^2 \theta)^2 + \frac{g}{2} \tilde{\rho}^2$$

Completing the path integral over  $\tilde{\rho}$ , we obtain to leading order in  $\theta$

$$L_\theta = \frac{1}{2g} (\partial_\tau \theta)^2 + \frac{\alpha}{4} \rho_0 (\partial_x \theta)^2 + \beta \rho_0 (\partial_x^2 \theta)^2.$$

The mean field correlation length exponent  $\nu = 1/2$  can be derived from the spatial scaling symmetry with  $\partial_\tau \theta = 0$ :

$$\alpha \rightarrow \lambda^{-1}\alpha, x \rightarrow \lambda^\nu x.$$

At the critical point  $\alpha = 0$ , the dynamical critical exponent  $z = 2$  is determined by applying the following scaling transformation to the effective Lagrangian  $L_\theta$ ,

$$x \rightarrow \lambda x, t \rightarrow \lambda^z t,$$

and noting that  $L_\theta$  is invariant when  $z = 2$ , except for an overall multiplicative factor  $\lambda^{-4}$ . Notably  $z = 2$  results from the dominance of the quartic term  $\beta|\partial_x^2\Psi|^2$  at the critical point.

Given  $z = 2$  and  $\nu = 1/2$ , the Kibble-Zurek temporal and spatial exponents from Eqs. 2 and 3 are given by  $a = 1/2$  and  $b = 1/4$ , respectively. In our treatment of the Kibble-Zurek mechanism, we neglect the trap because the critical shaking amplitude  $s_c$  is primarily determined by the homogeneous kinetic energy term instead of the interactions which are more sensitive to the density profile in the trap. The results are consistent with our measured values of  $a_{ex} = 0.50(2)$  and  $b_{ex} = 0.26(2)$  within our experimental uncertainty. The consistency of our results with the mean-field exponents contrasts with experiments near the classical Bose-condensation phase transition, which could only be explained by beyond-mean-field exponents (15,16). This difference may result from the effectively ferromagnetic quantum phase transition in our system being in a different universality class from Bose-condensation, even though the mean-field exponents are the same for both transitions. Moreover, it is expected that there are beyond-mean-field corrections to the critical exponents, but the corrections appear to be smaller than we can resolve with the present experiments.

To determine the constraints on  $z$  and  $\nu$  presented in Fig. 3F, we first calculate the relative likelihood of different values of the dynamic exponents ( $a$  and  $b$ ) based on the reduced chi-squared values for using power-laws to explain the experimental data in 2D and 3C. We use Eqs. 2 and 3 to convert the likelihood of the dynamic exponents into the likelihood of the equilibrium exponents, from which we determine the confidence intervals.

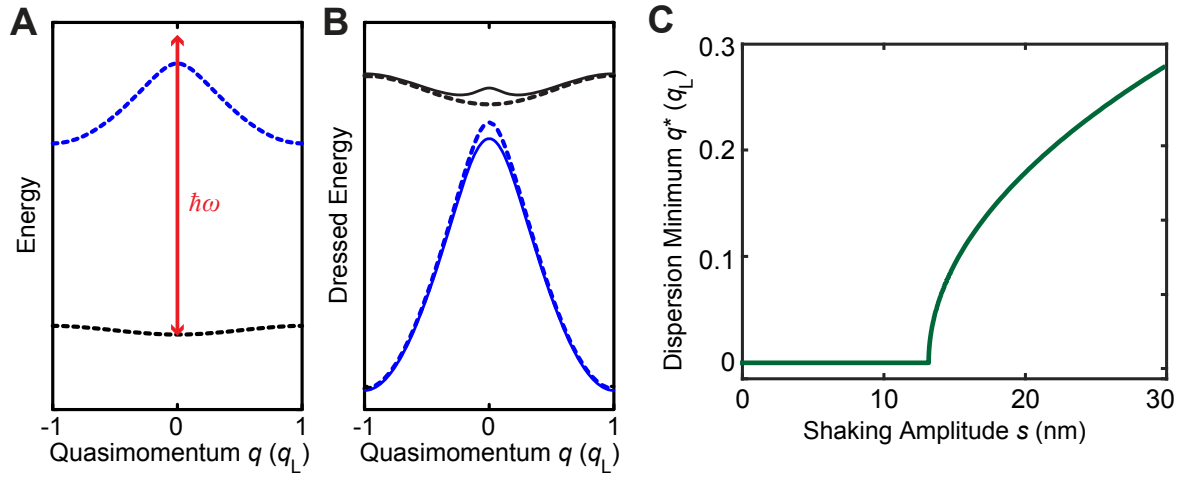


**Fig. S1**

Modification of band structure by shaking the lattice. **(A)** An illustration shows how shaking the lattice at a frequency  $\omega$  slightly greater than the band gap at  $q = 0$  couples the ground band (black dashed curve) to the first excited band (blue dashed curve). The lattice momentum is  $q_L = h/\lambda$  where  $\lambda = 1064$  nm is the wavelength of the lattice laser. **(B)** In a dressed picture the coupling leads to level repulsion between the bands which results in modified energy bands (solid curves). With sufficient shaking amplitude the ground band (black) develops a double well with minima at  $q = \pm q^*$ . **(C)** The ground band minimum  $q^*$  is calculated from the Floquet theory based on our experimental parameters. Above the critical point  $s > s_c$ ,  $q^*$  closely follows the threshold law  $q^* \propto (s - s_c)^{1/2}$  in the plotted range.

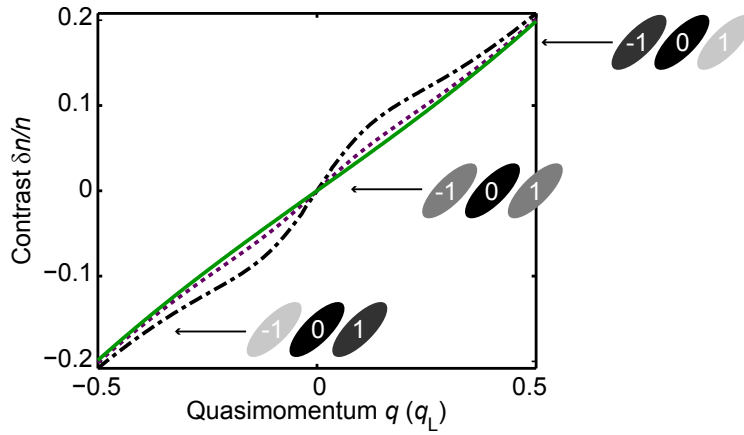


**Fig. S2**

Detection of quasimomentum via density deviation. The contrast  $\delta n/n$  between the  $\pm 1$  Bragg peaks can be used to assess the quasimomentum  $q$ , according to a calculation of the Floquet eigenstates in the shaken lattice (28). The contrast only weakly depends on shaking amplitude, shown for  $s = 0$  (solid),  $s = s_c$  (dotted), and  $s = 2s_c$  (dot-dashed). The illustrations represent the density in the three relevant Bragg peaks after time-of-flight.

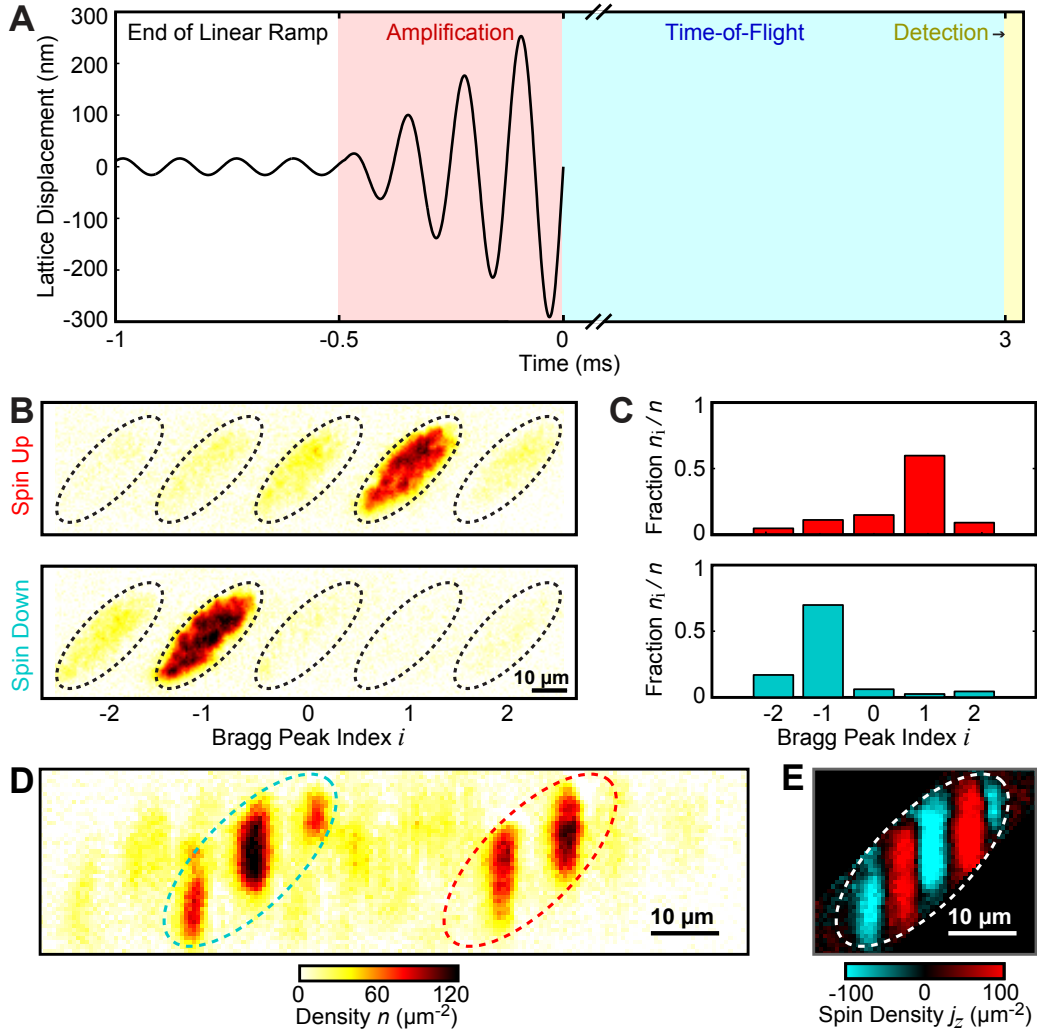


**Fig. S3**

Detection and reconstruction of ferromagnetic domains. (A) We amplify the distinction between the pseudo-spin states by rapidly increasing the shaking amplitude over 0.5 ms before time-of-flight (TOF). After 3 ms TOF we detect the density distribution by absorption imaging. The examples shown in this figure correspond to  $s = 32$  nm before amplification. (B) Sample images used to calibrate the occupation of each Bragg peak are taken with all of the atoms in pseudo-spin up (top) or down (bottom). Ellipses identify the Bragg peaks. For these images we use a longer TOF lasting 5 ms. Each spin predominantly occupies a different Bragg peak. (C) The fraction of density  $n_i/n$  in each Bragg peak distinguishes spin up (top) and down (bottom). (D) A sample image shows the density distribution after 3 ms TOF for a condensate with five domains. The ellipses mark the two most important Bragg peaks and are colored to indicate the spin state which dominates each peak. (E) Reconstruction based on the fractions in panel C produces the spin density distribution corresponding to the TOF image in panel D.

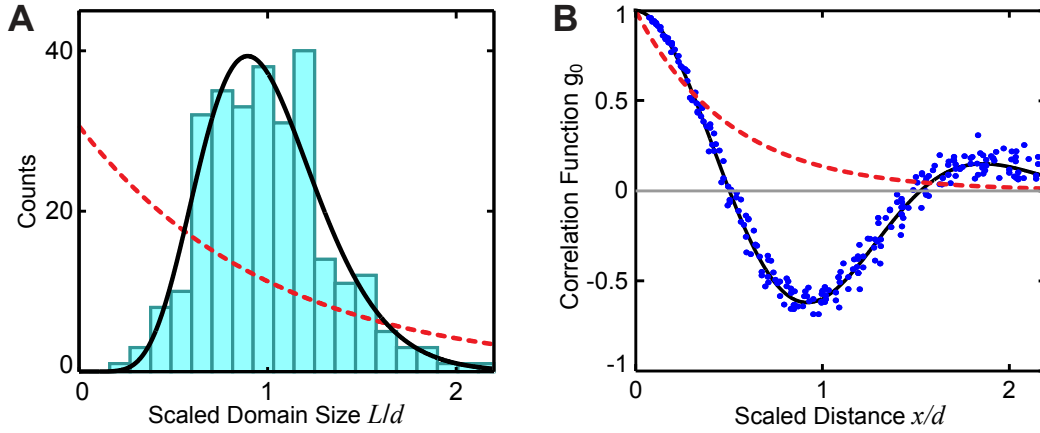


**Fig. S4**

Sub-Poisson generation of domain walls. **(A)** The distribution of domain sizes  $L$  for 110 samples with quench rate  $\dot{s} = 0.08$  nm/ms is bunched near the average domain size  $d$ . The solid curve shows a fit based on the function  $A(L/d)^{a-1}e^{-aL/d}$ , where the coefficient  $A = a^a/\Gamma(a)$ , which interpolates between the exponential ( $a = 1$ ) and delta ( $a \rightarrow \infty$ ) distributions. The fit yields  $a = 10(1)$  for the measured distribution. For comparison, the dashed curve shows an exponential distribution ( $a = 1$ ) corresponding to Poisson generation of defects. **(B)** Poisson generation of defects would lead to exponential decay of spin correlations as  $g_P(x) = e^{-2x/d}$  (dashed curve), which does not exhibit the anti-correlation seen in the data from Fig. 3E (blue points). The solid curve shows the fit to the measured correlations based on Eq. 7.

## References and Notes

1. W. H. Zurek, Cosmological experiments in superfluid helium? *Nature* **317**, 505–508 (1985). [doi:10.1038/317505a0](https://doi.org/10.1038/317505a0)
2. I. Chuang, R. Durrer, N. Turok, B. Yurke, Cosmology in the laboratory: Defect dynamics in liquid crystals. *Science* **251**, 1336–1342 (1991). [doi:10.1126/science.251.4999.1336](https://doi.org/10.1126/science.251.4999.1336) [Medline](#)
3. S. L. Veatch, O. Soubias, S. L. Keller, K. Gawrisch, Critical fluctuations in domain-forming lipid mixtures. *Proc. Natl. Acad. Sci. U.S.A.* **104**, 17650–17655 (2007). [doi:10.1073/pnas.0703513104](https://doi.org/10.1073/pnas.0703513104) [Medline](#)
4. T. W. B. Kibble, Topology of cosmic domains and strings. *J. Phys. Math. Gen.* **9**, 1387–1398 (1976). [doi:10.1088/0305-4470/9/8/029](https://doi.org/10.1088/0305-4470/9/8/029)
5. Q. Zhou, T. L. Ho, Signature of quantum criticality in the density profiles of cold atom systems. *Phys. Rev. Lett.* **105**, 245702 (2010). [doi:10.1103/PhysRevLett.105.245702](https://doi.org/10.1103/PhysRevLett.105.245702) [Medline](#)
6. A. Polkovnikov, K. Sengupta, A. Silva, M. Vengalattore, *Colloquium* : Nonequilibrium dynamics of closed interacting quantum systems. *Rev. Mod. Phys.* **83**, 863–883 (2011). [doi:10.1103/RevModPhys.83.863](https://doi.org/10.1103/RevModPhys.83.863)
7. A. del Campo, W. H. Zurek, Universality of phase transition dynamics: Topological defects from symmetry breaking. *Int. J. Mod. Phys. A* **29**, 1430018 (2014). [doi:10.1142/S0217751X1430018X](https://doi.org/10.1142/S0217751X1430018X)
8. M. Kolodrubetz, B. K. Clark, D. A. Huse, Nonequilibrium dynamic critical scaling of the quantum Ising chain. *Phys. Rev. Lett.* **109**, 015701 (2012). [doi:10.1103/PhysRevLett.109.015701](https://doi.org/10.1103/PhysRevLett.109.015701) [Medline](#)
9. A. Chandran, A. Erez, S. S. Gubser, S. L. Sondhi, Kibble-Zurek problem: Universality and the scaling limit. *Phys. Rev. B* **86**, 064304 (2012). [doi:10.1103/PhysRevB.86.064304](https://doi.org/10.1103/PhysRevB.86.064304)
10. A. Francuz, J. Dziarmaga, B. Gardas, W. H. Zurek, Space and time renormalization in phase transition dynamics. *Phys. Rev. B* **93**, 075134 (2016). [doi:10.1103/PhysRevB.93.075134](https://doi.org/10.1103/PhysRevB.93.075134)
11. I. Bloch, J. Dalibard, W. Zwerger, Many-body physics with ultracold gases. *Rev. Mod. Phys.* **80**, 885–964 (2008). [doi:10.1103/RevModPhys.80.885](https://doi.org/10.1103/RevModPhys.80.885)
12. J. Dziarmaga, Dynamics of a quantum phase transition and relaxation to a steady state. *Adv. Phys.* **59**, 1063–1189 (2010). [doi:10.1080/00018732.2010.514702](https://doi.org/10.1080/00018732.2010.514702)
13. C. N. Weiler, T. W. Neely, D. R. Scherer, A. S. Bradley, M. J. Davis, B. P. Anderson, Spontaneous vortices in the formation of Bose–Einstein condensates. *Nature* **455**, 948–951 (2008). [doi:10.1038/nature07334](https://doi.org/10.1038/nature07334)
14. G. Lamporesi, S. Donadello, S. Serafini, F. Dalfovo, G. Ferrari, Spontaneous creation of Kibble–Zurek solitons in a Bose–Einstein condensate. *Nat. Phys.* **9**, 656–660 (2013). [doi:10.1038/nphys2734](https://doi.org/10.1038/nphys2734)

15. L. Corman, L. Chomaz, T. Bienaimé, R. Desbuquois, C. Weitenberg, S. Nascimbène, J. Dalibard, J. Beugnon, Quench-induced supercurrents in an annular Bose gas. *Phys. Rev. Lett.* **113**, 135302 (2014). [doi:10.1103/PhysRevLett.113.135302](https://doi.org/10.1103/PhysRevLett.113.135302) [Medline](#)
16. N. Navon, A. L. Gaunt, R. P. Smith, Z. Hadzibabic, Quantum gases. Critical dynamics of spontaneous symmetry breaking in a homogeneous Bose gas. *Science* **347**, 167–170 (2015). [doi:10.1126/science.1258676](https://doi.org/10.1126/science.1258676) [Medline](#)
17. L. E. Sadler, J. M. Higbie, S. R. Leslie, M. Vengalattore, D. M. Stamper-Kurn, Spontaneous symmetry breaking in a quenched ferromagnetic spinor Bose-Einstein condensate. *Nature* **443**, 312–315 (2006). [doi:10.1038/nature05094](https://doi.org/10.1038/nature05094) [Medline](#)
18. K. Baumann, R. Mottl, F. Brennecke, T. Esslinger, Exploring symmetry breaking at the Dicke quantum phase transition. *Phys. Rev. Lett.* **107**, 140402 (2011). [doi:10.1103/PhysRevLett.107.140402](https://doi.org/10.1103/PhysRevLett.107.140402) [Medline](#)
19. D. Chen, M. White, C. Borries, B. DeMarco, Quantum quench of an atomic Mott insulator. *Phys. Rev. Lett.* **106**, 235304 (2011). [doi:10.1103/PhysRevLett.106.235304](https://doi.org/10.1103/PhysRevLett.106.235304) [Medline](#)
20. E. Nicklas, M. Karl, M. Höfer, A. Johnson, W. Muessel, H. Strobel, J. Tomkovič, T. Gasenzer, M. K. Oberthaler, Observation of scaling in the dynamics of a strongly quenched quantum gas. *Phys. Rev. Lett.* **115**, 245301 (2015). [doi:10.1103/PhysRevLett.115.245301](https://doi.org/10.1103/PhysRevLett.115.245301) [Medline](#)
21. S. Braun, M. Friesdorf, S. S. Hodgman, M. Schreiber, J. P. Ronzheimer, A. Riera, M. Del Rey, I. Bloch, J. Eisert, U. Schneider, Emergence of coherence and the dynamics of quantum phase transitions. *Proc. Natl. Acad. Sci. U.S.A.* **112**, 3641–3646 (2015). [Medline](#)
22. C. Meldgin, U. Ray, P. Russ, D. Chen, D. M. Ceperley, B. DeMarco, Probing the Bose glass–superfluid transition using quantum quenches of disorder. *Nat. Phys.* **12**, 646–649 (2016). [doi:10.1038/nphys3695](https://doi.org/10.1038/nphys3695)
23. M. Anquez, B. A. Robbins, H. M. Bharath, M. Boguslawski, T. M. Hoang, M. S. Chapman, Quantum Kibble-Zurek mechanism in a spin-1 Bose-Einstein condensate. *Phys. Rev. Lett.* **116**, 155301 (2016). [doi:10.1103/PhysRevLett.116.155301](https://doi.org/10.1103/PhysRevLett.116.155301) [Medline](#)
24. N. Gemelke, E. Sarajlic, Y. Bidel, S. Hong, S. Chu, Parametric amplification of matter waves in periodically translated optical lattices. *Phys. Rev. Lett.* **95**, 170404 (2005). [doi:10.1103/PhysRevLett.95.170404](https://doi.org/10.1103/PhysRevLett.95.170404) [Medline](#)
25. H. Lignier, C. Sias, D. Ciampini, Y. Singh, A. Zenesini, O. Morsch, E. Arimondo, Dynamical control of matter-wave tunneling in periodic potentials. *Phys. Rev. Lett.* **99**, 220403 (2007). [doi:10.1103/PhysRevLett.99.220403](https://doi.org/10.1103/PhysRevLett.99.220403) [Medline](#)
26. J. Struck, C. Ölschläger, M. Weinberg, P. Hauke, J. Simonet, A. Eckardt, M. Lewenstein, K. Sengstock, P. Windpassinger, Tunable gauge potential for neutral and spinless particles in driven optical lattices. *Phys. Rev. Lett.* **108**, 225304 (2012). [doi:10.1103/PhysRevLett.108.225304](https://doi.org/10.1103/PhysRevLett.108.225304) [Medline](#)
27. J. Struck, C. Ölschläger, R. Le Targat, P. Soltan-Panahi, A. Eckardt, M. Lewenstein, P. Windpassinger, K. Sengstock, Quantum simulation of frustrated classical magnetism in triangular optical lattices. *Science* **333**, 996–999 (2011). [doi:10.1126/science.1207239](https://doi.org/10.1126/science.1207239) [Medline](#)

28. C. V. Parker, L.-C. Ha, C. Chin, Direct observation of effective ferromagnetic domains of cold atoms in a shaken optical lattice. *Nat. Phys.* **9**, 769–774 (2013).  
[doi:10.1038/nphys2789](https://doi.org/10.1038/nphys2789)
29. G. Jotzu, M. Messer, R. Desbuquois, M. Lebrat, T. Uehlinger, D. Greif, T. Esslinger, Experimental realization of the topological Haldane model with ultracold fermions. *Nature* **515**, 237–240 (2014). [doi:10.1038/nature13915](https://doi.org/10.1038/nature13915) [Medline](#)
30. W. Zheng, B. Liu, J. Miao, C. Chin, H. Zhai, Strong interaction effects and criticality of bosons in shaken optical lattices. *Phys. Rev. Lett.* **113**, 155303 (2014).  
[doi:10.1103/PhysRevLett.113.155303](https://doi.org/10.1103/PhysRevLett.113.155303) [Medline](#)
31. L.-C. Ha, L. W. Clark, C. V. Parker, B. M. Anderson, C. Chin, Roton-maxon excitation spectrum of Bose condensates in a shaken optical lattice. *Phys. Rev. Lett.* **114**, 055301 (2015). [doi:10.1103/PhysRevLett.114.055301](https://doi.org/10.1103/PhysRevLett.114.055301) [Medline](#)
32. Materials and methods are available on *Science Online*.
33. J. Xu, S. Wu, X. Qin, J. Huang, Y. Ke, H. Zhong, C. Lee, Kibble-Zurek dynamics in an array of coupled binary Bose condensates. *Europhys. Lett.* **113**, 50003 (2016).  
[doi:10.1209/0295-5075/113/50003](https://doi.org/10.1209/0295-5075/113/50003)
34. S. Choudhury, E. J. Mueller, Transverse collisional instabilities of a Bose-Einstein condensate in a driven one-dimensional lattice. *Phys. Rev. A* **91**, 023624 (2015).  
[doi:10.1103/PhysRevA.91.023624](https://doi.org/10.1103/PhysRevA.91.023624)
35. C.-L. Hung, X. Zhang, L.-C. Ha, S.-K. Tung, N. Gemelke, C. Chin, Extracting density–density correlations from *in situ* images of atomic quantum gases. *New J. Phys.* **13**, 075019 (2011). [doi:10.1088/1367-2630/13/7/075019](https://doi.org/10.1088/1367-2630/13/7/075019)